Finite-Element Analysis of the Rotor/Stator Contact in a Ring-Type Ultrasonic Motor

Takashi Maeno, Takayuki Tsukimoto, and Akira Miyake

Abstract—**A new way to understand mechanical characteristics of an ultrasonic motor by using a finite-element (FE) analysis is presented. First, the vibration mode of a stator by using a finite-element method (FEM) code is calculated. The path of the elliptic motion of the stator's teeth is obtained. The computed vibration mode at the surface of the stator is compared with the measured one by using an electrooptical displacement transducer. Next, the contact condition of the rotor/stator is calculated. The stick/slip behavior at the contact interface of the rotor/stator is taken into account. The displacement and velocity of the rotor/stator, the distribution of the stick/slip area, the rotational speed of the rotor, and the friction loss of the motor are obtained. The calculated rotor displacement and torque-rotational speed (T–N) curve correspond closely to the experimentally measured ones. Furthermore, an internal loss of the rotor/stator and the loss of the supporting felt is measured. The total loss of the motor obtained by adding the aforementioned losses and the calculated friction loss agree with the measured total loss. The calculated and the measured efficiency of the motor also agree.**

I. Introduction

THE ULTRASONIC MOTOR was invented by Sashida [1] in 1982. The principle of the ultrasonic motor is based on two energy transfers. First is the transfer from electric power to a mechanical vibrational power by piezoelectric ceramics employed in the stator (vibrating body) to induce traveling or standing waves in the stator with frequencies in the ultrasonic range. Secondly, the wave energy in the stator is transferred to the rotor/slider (driven body) by means of the frictional contact force between them. This replaces the electromagnetic force that usual electromagnetic motors have utilized. The ultrasonic motor has been of interest in industry because of its unique characteristics such as its output power per unit volume, high stationary limiting torque, high maximum operating torque, simple design, silence, and high precision controllability.

Several types of ultrasonic motors have been proposed [1]–[6]. They can be divided into two groups according to their contact principles between the stator and the rotor/slider. One is a "traveling" contact type, in which the contact area between the stator and rotor/slider moves with the traveling wave excited in the stator. The two bodies are always in contact near the wave crests. The other is an "intermittent" contact type, in which the two bodies contact intermittently and the contact area of the stator always remains the same. One example has contact controlled by synchronized forced vibration of the stator in the normal and tangential direction.

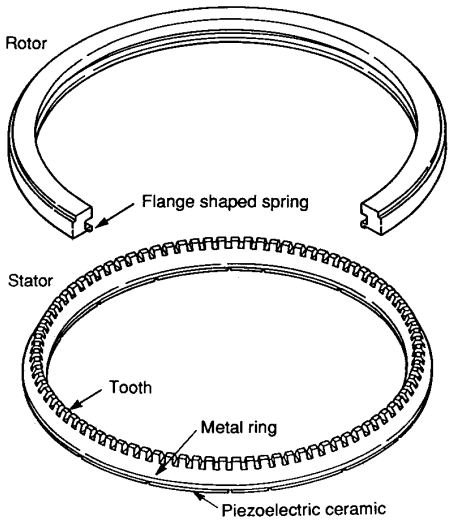

Fig. 1. The rotor and stator of a ring-type ultrasonic motor.

A ring-type motor developed and produced by Canon, Inc. for autofocus lenses [5], [6], which fits the design of the lens unit, employs the traveling wave (See Fig. 1). The traveling wave is excited in the stator ring by disjoined conductor films on a piezoelectric ceramic bonded to one side of the stator. There are teeth on the another side of the stator to enlarge the tangential velocity at the contact interface. A flange-shaped rotor spring contacts the stator's teeth at the crests of the stator's traveling waves. The rotor, which is pressed against the stator with a certain normal force, is driven in the opposite direction from the stator's traveling wave movement by means of the friction force at the contact areas as shown schematically in Fig. 2.

One of the most important points for designing the ultrasonic motor is the control of the dynamic contact behavior between the two bodies. In order to understand the contact characteristics, various researchers have undertaken theoretical and experimental studies in recent years. Ueha and Kurosawa [7] were the first to analyze the rotor/stator

Manuscript received January 14, 1992; revised May 11, 1992; accepted May 26, 1992.

T. Maeno was with the Computer Mechanics Laboratory, Department of Mechanical Engineering, University of California, Berkeley, CA 94720, and is now with Canon, Inc., 3-30-2, Shimomaruko, Ohta-ku, Tokyo 146, Japan.

T. Tsukimoto is with Canon, Inc., 3-30-2, Shimomaruko, Ohta-ku, Tokyo 146, Japan.

A. Miyake is with the Canon Research Center, 5-1 Wakamiya, Morinosato Atsugi, Kanagawa 243–01, Japan.

IEEE Log Number 9203442.

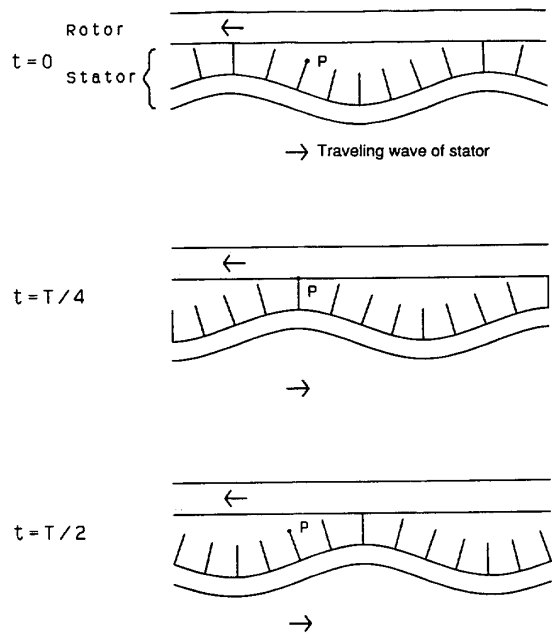

Fig. 2. Principles to drive the ultrasonic motor.

interface. They introduced a linear spring model for the rotor's normal deformation and used it to calculate the motor's performance, such as the torque–rotational speed (T–N) curve and motor efficiency. Yamabuchi and Kagawa [8] analyzed the piezoelectric elastic structures using the finite-element method (FEM) and proposed an equivalent electrical circuit. They showed ways to understand qualitatively the motor's characteristics. However, the details of the mechanical contact behavior of the two bodies, such as the nonlinearity of contact and the shear deformation of bodies near the contact areas, were not considered in the above studies.

In our research, we clarify the mechanical characteristics of the ring type ultrasonic motor by using FE codes. First, the vibration mode of the actual ring-type stator is calculated by using the FE code MSC/NASTRAN. Next, the elastic contact of the rotor/stator, considering the shear deformation of bodies by using a static friction coefficient μ_s and a dynamic friction coefficient μ_d, is simulated by the FE code JNIKE3D. A complex distribution of the stick and slip areas within the contact region is shown. Important motor performances, including the T–N curve, power loss, and efficiency, are calculated as well. By considering the initial displacement of the rotor/stator, we obtain results that are in good agreement with the experimental results.

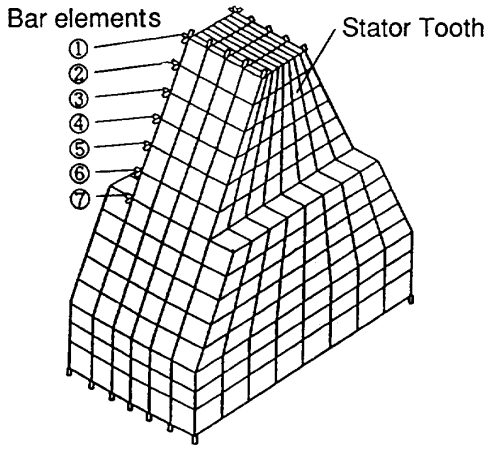

Fig. 3. Finite-element model of the stator.

II. Stator Vibration

The stator vibration modes of the ring-type ultrasonic motor have been calculated by using the simple bending model of a bar [6]. But the actual stator has a complex shape as shown in Fig. 1. As the cross section of the stator is trapezoidal and it has teeth, it is difficult to predict the shape of the stator traveling wave by means of the previous method. So, we calculate the stator vibration mode by using a FE code. Fig. 3 shows the finite-element model of the stator. One tooth, in other words, 1/90 of the stator along the circumferential direction is modeled. It has 837 nodes and 576 solid elements. Bar elements fixed at the edge of the tooth represent thin stainless plates used as targets in the optical measurement. Two natural modes, the sine/cosine modes, which have the same mode shapes and natural frequencies, and their frequencies are calculated by utilizing the cylindrical symmetry solution sequence of the MSC/NASTRAN. The calculated natural modes are standing waves. The two standing waves at any point in the stator have the following forms, shown at the bottom of the page in (1), where, A_n and A_t are normal and tangential amplitudes, respectively, ω is the angular velocity, t is time, n is a nodal diameter, θ is the circumferential coordinate angle, and ϕ is the phase delay due to the existence of the teeth. A_n, A_t, and ϕ are functions of the location of the selected point. If the stator did not have the periodic thickness change due to the presence of the teeth, the value of ϕ would be zero. We can obtain the traveling wave form by adding the above two standing waves. The normal and tangential deformations at any point in the stator, w_n and w_t, are

$$w_n = w_{ns} + w_{nc} = A_n \cos(\omega t - n\theta)$$
$$w_t = w_{ts} + w_{tc} = A_t \sin(\omega t - n\theta - \phi) \quad (2)$$

$$w_{ns} = A_n \sin(\omega t)\sin(n\theta) \text{ (normal deformation of sine mode)}$$
$$w_{ts} = -A_t \sin(\omega t)\cos(n\theta + \phi) \text{ (tangential deformation of sine mode)}$$
$$w_{nc} = A_n \cos(\omega t)\cos(n\theta) \text{ (normal deformation of cosine mode)}$$
$$w_{tc} = A_t \cos(\omega t)\sin(n\theta + \phi) \text{ (tangential deformation of cosine mode)} \quad (1)$$

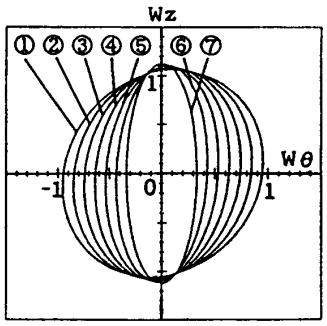

Fig. 4. The elliptic motion of some points on the teeth.

Equation (2) shows that any point in the stator moves elliptically when the traveling wave is excited. Fig. 4 shows the elliptic motion of some nodes when the seventh traveling wave is excited in the stator. Circled numbers of each ellipse correspond to the nodes shown in the Fig. 3. This figure shows that the tangential displacement is enlarged at the top of the teeth. It also shows that the axis of the ellipses are not vertical, in other words, ϕ is not zero, at the edge of the tooth due to the existence of the tooth. Fig. 5 shows the comparison between the calculated and the measured normal and tangential amplitudes. Measurement of vibrational amplitudes on the target plates bonded at the edge of some teeth was made by utilizing an electrooptical displacement transducer made by Zimmer KG [9]. The measured amplitudes of different teeth, plotted by using solid lines, are distributed because the amplitudes of the sine and cosine modes are not the same in the actual motor. The calculated amplitude, a broken line, is in the middle of the measured lines. This result shows that this FE analysis gives an appropriate solution, in opposition to the beam model approximation that had an error for predicting the vibrational modes of the complex shaped stator.

III. Rotor/Stator Contact

A. Analysis Model

We calculate the dynamic contact behavior of the rotor/stator by using the finite-element code JNIKE3D. This code has the ability to treat the contact problem based on a penalty function formulation [10]. For solving the contact problem, we can consider the static/dynamic contact condition. In other words, we can define the static/dynamic friction coefficient as a function of the relative velocity between the two bodies.

The condition of the frictional contact is described shortly as follows. Surfaces of finite elements that can contact are defined as so-called "master" and "slave" surfaces. Fig. 6 shows the slave node S_n on the master segment M_1, M_2, M_3, and M_4 when S_n contacts the master surface. Linear springs from S_n to M_1, M_2, M_3, and M_4 are imagined in the normal and tangential directions. The normal force is added in the normal spring in order to place the point S_n on the master segment. When S_n does not contact the master segment, the normal and the tangential springs are removed.

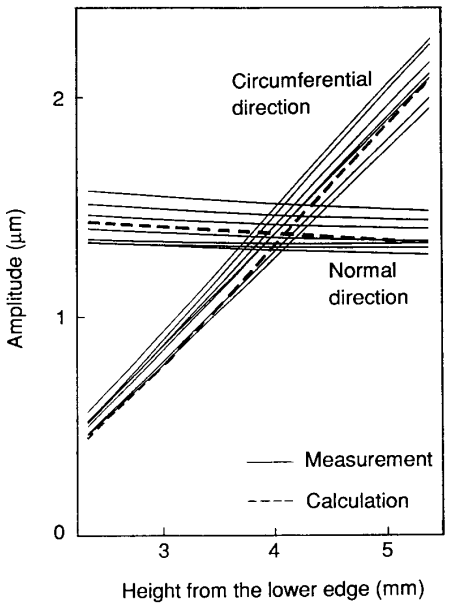

Fig. 5. Normal and tangential amplitude of the stator at the outside edge of the teeth.

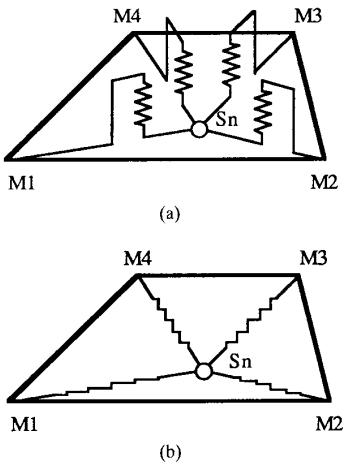

Fig. 6. Springs in the master/slave interface. (a) Normal springs. (b) Tangential springs.

When the point S_n sticks, the tangential force vector F_t is applied in the tangential springs to keep the point Sn at the same place in the master segment with the result of the previous time step. Now, the maximum steady friction force $F_{\max}$ is

$$F_{\max} = \mu_s N \tag{3}$$

where μ_s is a static friction coefficient, N is a normal force of point Sn. If the tangential force vector satisfies

$$|F_t| \leq F_{\max} \tag{4}$$

then, the point S_n sticks. The relative location of S_n to the master surface does not change during this time step. On the

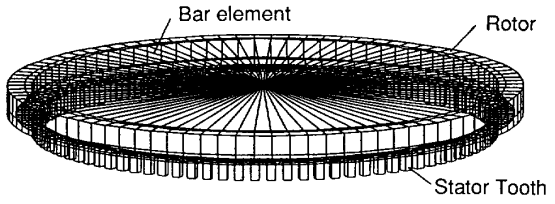

Fig. 7. The finite-element model of the rotor/stator for the contact analysis.

other hand, if the tangential force vector is

$$|F_t| > F_{\max} \tag{5}$$

then, the point S_n slips. Then F_t is replaced by the following slipping force vector, F_t^s,

$$F_t^s = \mu_d N \frac{F_t}{|F_t|} \tag{6}$$

where, μ_d is a dynamic friction coefficient as a function of a relative velocity between S_n and the master segment. So, the dynamic friction force is applied at this point S_n. Calculation is repeated by changing the normal force vector F_n for contact and the tangential force vector F_t for stick/slip, to obtain the converged solution for every time step in which the displacement and energy norm is smaller than the given tolerances.

A mesh model is shown in Fig. 7. The change of the vibration mode of the stator's ring due to the rotor contact was not observed by the measurement using the electrooptical displacement transducer because the change was smaller than the resolution of the measurement. We can say that the deformation of the stator's ring due to the rotor contact is negligible. So only the teeth are modeled by using solid elements to express the shear deformation of the stator. The rotor is modeled using solid and shell elements. Shell elements are used for the flange-shaped spring in order to increase the accuracy and reduce the mesh size. The materials of the rotor and stator are aluminum and invar, respectively. Bar elements are connected at the inner edge of the rotor in order to constrain the rotor in the radial direction. The rotor/stator deformations and the force distributions were steady after about the fifth step. The calculation is performed up to the 15th step and the results are averaged over the sixth to 15th steps to increase the accuracy. The elliptical motion of the stator (traveling wave) with frequency of 30 kHz is given as a forced deformation in the radial, tangential, and normal directions at the downside nodes of the teeth from the first step. The rotor pressure is given at the top surface of the rotor ring as concentrated loads from the first step as well. Load torque is given at the inner side of the rotor ring from the second step as the concentrated load in the circumferential direction. The inertial force is ignored because the natural frequencies of the rotor spring and the stator teeth are designed to be high compared with the exciting frequency of the stator. The time step Δt is 5×10^{-7} (s). This value is selected so that the change of the stator deformation through one step is sufficiently small.

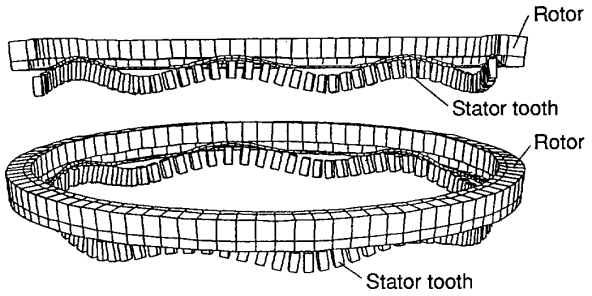

Fig. 8. Deformation of the rotor/stator.

We also calculate the power loss by friction, W_f from the result of the FE analysis as

$$W_f = \sum_{i=1}^{N} (f_i |v_{si} - v_{ri}|) \tag{7}$$

where, i is a node on the rotor/stator, f_i is a tangential force at the slipping node i, v_{si} and v_{ri} are tangential velocities of the stator and rotor at point i, respectively. Actually, the rotor/stator nodes are not located at the same point i, so linear interpolation is applied. Internal loss near the contact interface due to the frictional contact is ignored.

A Hitachi super computer S820 was used for the calculation. The CPU time for calculating one case is about 60 min (VPU (vectorized calculation time per unit) is about 40 min).

B. Comparison between the Calculated and the Experimentally Measured Results

Fig. 8 shows the deformation of the rotor/stator calculated by the JNIKE3D FE code. The rotor springs are bent by the contact force between the rotor/stator and contact at the crest of the stator traveling wave. We can see that there are certain contact areas.

Fig. 9(a) shows the normal displacements of the stator teeth and the rotor spring, where the stator vibration amplitude is 2 $\mu mp - p$, the rotor load in the normal direction is 14 N, and the load torque is zero Nm. The horizontal axis is the circumferential location of the interface nodes. Lines (a) and (b) represent the displacements at the inner and outer edges in the interface area of the rotor spring, respectively. The displacement of the stator teeth are shown in bar-graph form with one side on the zero displacement line. This figure shows that the crest of the stator's traveling wave penetrates to the rotor spring with contact along the outer line (b). Three or four teeth per one wave contact the rotor spring. Fig. 9(b) shows the measured deformations of the rotor/stator by using the electro optical displacement transducer [9]. The horizontal axis is time. The rotor and stator deformation were measured separately, but are shown simultaneously. This figure also shows that the rotor contacts the stator at the crest of the stator's traveling wave. The calculated and measured shape of the rotor deformation correspond closely.

Fig. 10(a) shows the normal force of the rotor/stator contact. Fig. 10(b) and (c) show the tangential force of the rotor/stator when the torque is 0 and 0.05 Nm, respectively. When the load

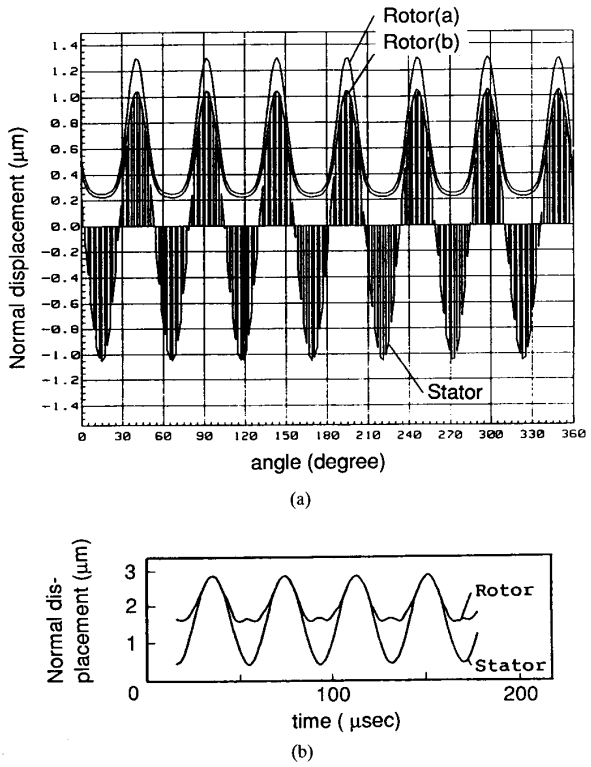

Fig. 9. Normal displacement of the rotor/stator interface. (a) Calculation. (b) Measurement.

torque is zero, the resultant tangential force is zero, which does not mean that the friction forces at every point is zero. This means that the resultant forces in the positive and the negative directions have the same value. On the contrary, when the load torque is applied, the resultant of the tangential force is not zero, but must balance the applied load torque.

Fig. 11 shows the time dependent change of the tangential force at a certain node on the rotor surface. We can see an interesting stick/slip phenomena due to the periodic change of the stator's tangential speed and the shear deformation of the rotor/stator. When the node on the rotor starts contacting the stator, the tangential speed of the stator is lower than that of the rotor. Consequently, the rotor/stator interface slips at a certain velocity. The direction of the dynamic friction force in the rotor is negative and the value is proportional to the normal force ($f = \mu_d N$, μ_d : dynamic friction coefficient) . At a later time when the speeds of the rotor/stator nodes become the same, the interface area sticks. At this time, the static friction force f is smaller than the maximum steady friction force $f_{\max}$ ($f_{\max} = \mu_s N$: μ_s: static friction coefficient). After that, the stator speed exceeds the rotor speed and the interface area slips again. During this slip, the friction force at the rotor node has a positive value because the slip direction is different from the previous slip. After that, the rotor/stator speed becomes the same again and the interface area sticks again. Later, the stator speed becomes lower again and slips. The direction of the friction force becomes negative again. Finally, the rotor/stator interface breaks contact.

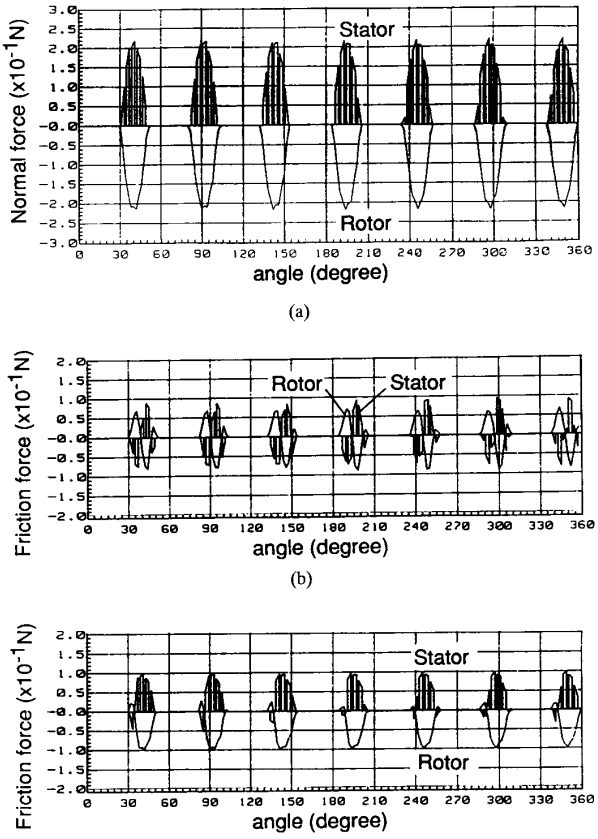

Fig. 10. Normal and tangential force between the stator and rotor. (a) Normal force. (b) Tangential force ($T = 0.0$ (Nm)). (c) Tangential force ($T = 0.005$(Nm)).

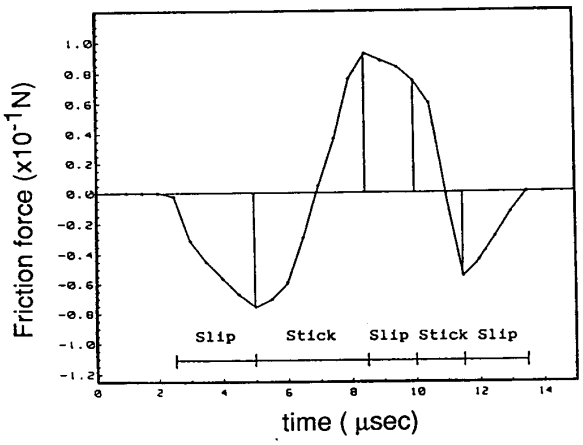

Fig. 11. The friction force at one point on the rotor interface.

These stick/slip phenomena are similar to the contact between two rollers that have different elastic moduli as analyzed by Bentall and Johnson [11]. The rotor corresponds to the soft roller and the stator to the hard one. One difference is that the hard roller's shape is a circle, but the stator's deformation is a sine function.

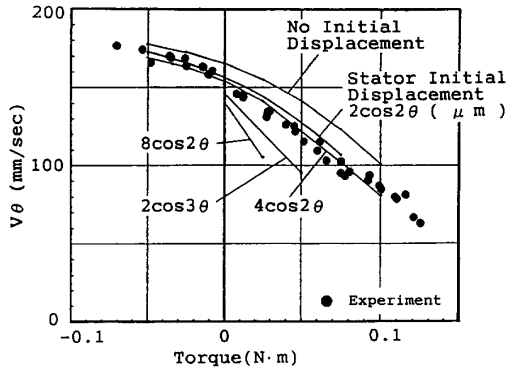

Fig. 12. T–N curve.

Fig. 12 shows the calculated and the measured torque–rotational speed (T–N) curves. The static and dynamic friction coefficients used in the calculation are 0.48 and 0.40, respectively. These values are selected so that slope of the calculated curve is in good agreement with the measured curve. The actual static and dynamic friction coefficients measured by the friction tester were 0.70 and 0.84, respectively. In order to explain these differences, future work should be done by considering some more effects on contact.

When there is no initial deformation of the rotor/stator, the calculated rotor speed is higher than that of the measurement. So, we introduce an out-of-plane initial deformation of the rotor/stator as can be observed. The initial deformation of the actual rotor/stator due to the tolerance of production has the shape

$$w = A\cos(n\theta). \tag{8}$$

Usually, $n = 2$ with an amplitude of a few microns is dominant in the actual ring type ultrasonic motor produced by Canon for auto focus lenses. The normal displacement of the rotor/stator when the initial deformation of the stator is $4\cos(2\theta)$ is shown in the Fig. 13. When there is this amount of the initial deformation, the calculated T–N curve corresponds with the measured one (see Fig. 12).

The friction loss W_f averaged from time step 6 to 15 is plotted in Fig. 14 with the measured internal loss of the rotor/stator and the loss of supporting members. The total power loss obtained by adding the above losses are in good agreement with a total loss that is directly measured. Accuracy of the calculated friction loss by using the equation (7) is confirmed.

The efficiency of the motor calculated by the above losses and a measured output power is compared with the measured one as well (see Fig. 15). The calculated and the measured efficiency are also in good agreement.

IV. Conclusion

We presented a new way to understand the mechanical characteristics of an ultrasonic motor by using FE analysis. First, we calculated the vibration mode of a stator by using a FE code MSC/NASTRAN. The shape of the elliptic motion at the surface of the stator's teeth obtained in the calculation

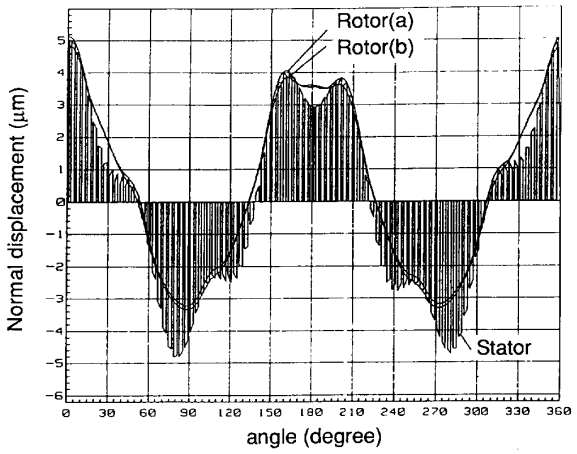

Fig. 13. Normal displacement of the rotor/stator when there is an initial deformation $4\cos(2\theta)$ (μ m).

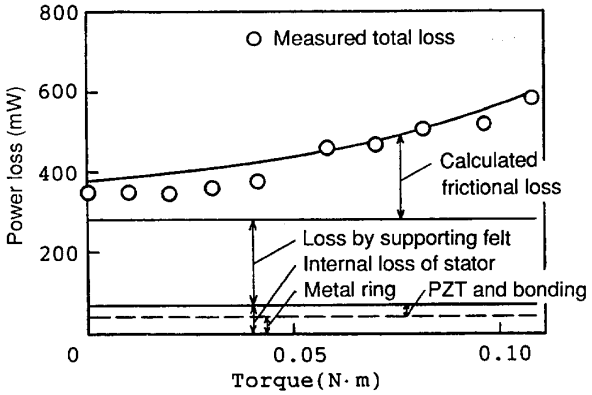

Fig. 14. The power loss of the motor.

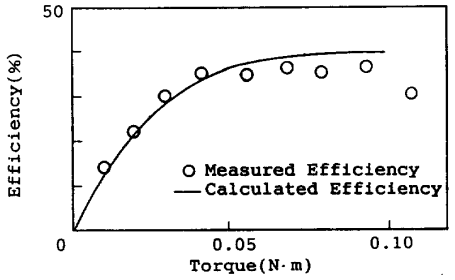

Fig. 15. The efficiency of the motor.

are in good agreement with the measured one. Next, we calculated the dynamic contact condition of the rotor/stator by using the FE code JNIKE3D. The displacement and the velocity of the rotor/stator, the distribution of the stick/slip area, the rotational speed of the rotor, and the friction loss of the motor are obtained. The calculated rotor displacement and T–N (torque-rotational speed) curve correspond closely to the experimentally measured ones. The calculated total loss and the efficiency of the motor agreed with the measured ones as well.

Future work should be done for the following reasons.

1) In this study, the friction coefficients, μ_s and μ_d, are selected so that the T–N curve corresponds to the experimentally measured one. These values of the friction coefficients are different from the measured values by using a friction tester. So the difference of the friction coefficient used in the calculation from the measured one should be clarified.
2) The calculated stick/slip condition of the rotor/stator contact presented in this study should be confirmed by experiments.
3) This study is done to clarify the mechanical characteristics of contact between the rotor/stator. This method should be used for obtaining the optimal design of the ultrasonic motor such as optimum stick/slip condition, the minimum frictional loss, and the maximum efficiency.

REFERENCES

[1] T. Sashida, "Trial construction and operation of an ultrasonic vibration driven motor," *Jpn. J. Appl. Phy.*, vol. 51, 1982, pp. 713 (in Japanese).
[2] Y. Ise, "Ultrasonic motor," *J. Acoust. Soc. Jpn.*, vol. 54–6, pp. 589, 1985 (in Japanese).
[3] A. Kumada, "A piezoelectric ultrasonic motor," *Jpn. J. Appl. Phys.*, vol. 24–2, p. 739, 1985.
[4] M. Kurosawa *et al.*, "An ultrasonic motor using bending vibration of a short cylinder," *IEEE Trans. Ultrason., Ferroelec., Freq. Contr.*, vol. 36, p. 517, 1989.
[5] K. Hosoe, "An application of ultrasonic motor for autofocus lenses," in *Proc. Touhoku Univ. Tsuuken Symp.*, 1989, p. 117 (in Japanese).
[6] I. Okumura and H. Mukohjima, "A structure of ultrasonic motor for autofocus lenses," in *Proc. Motor-Con '87*, 1987, p. 75.
[7] M. Kurosawa and S. Ueha, "Efficiency of ultrasonic motor using traveling wave," *J. Acoust. Soc. Jpn.*, vol. 44–1, p. 40, 1988 (in Japanese)
[8] T. Yamabuchi and Y. Kagawa, "Numerical simulation of a piezoelectric ultrasonic motor and its characteristics," *Simulation*, vol. 8–3, p. 69, 1989, (in Japanese)
[9] T. Tsukimoto *et al.*, "Measurement of ring type ultrasonic motor vibration" *Japan Soc. Appl. Phys.*, vol. 37, p. 329, 1990 (in Japanese)
[10] J. O. Hallqwist *et al.*, "Sliding interface with contact-impact in large scale lagrangian computations," *Comput. Methods Appl. Mech. Eng.*, vol. 51, p. 107, 1985.
[11] R. H. Bentall and K. L. Johnson, "Slip in the rolling contact of two dissimilar elastic rollers," *Int. J. Mech. Sci.*, vol. 10, p. 389, 1967.

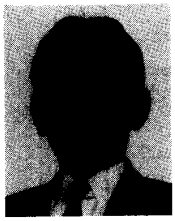

Takashi Maeno was born in Yamaguchi, Japan, on January 19, 1962. He received the B. Eng. and M. Eng. degrees in mechanical engineering from Tokyo Institute of Technology, Tokyo, Japan, in 1984 and 1986, respectively.

He has been working for the Production Engineering Research Laboratory of Canon Inc., Tokyo, Japan, since 1986. His major field of research is a mechanical vibration and tribology of precision mechanics including ultrasonic motors, VCR's, floppy disks, and paper transport systems. He has been a Visiting Industrial Fellow of the Computer Mechanics Laboratory at the University of California, Berkeley, since 1990. Since then, he has been doing research on computer simulation and the measurement of the dynamic contact in the ultrasonic motors.

Mr. Maeno is a member of the Japan Society of Mechanical Engineers.

Takayuki Tsukimoto was born in Kanagawa prefecture, Japan on Feb. 26, 1960. He received the B. Eng. degree in mechanical engineering in 1983 from Keio University, Tokyo, Japan.

He has been working for the Production Engineering Research Laboratory of Canon Inc., Tokyo, Japan since 1983. He has been engaged in the research and development of the ultrasonic motors. Since then, he has analyzed the fundamental characteristics and the squeal noises in the ring-type ultrasonic motors in 1989. His current research interest is to develop the small-sized and high performance ultrasonic motors.

Mr. Tsukimoto is a member of the Japan Society of Applied Physics.

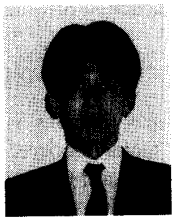

Akira Miyake was born in Okayama pref., Japan on November 17, 1960. He received the B.S. and M.S. degrees in physics from Osaka University, Osaka, Japan, in 1985 and 1987, respectively.

He has been working for Canon Research Center, Canon Inc., Japan, since 1987. He was engaged in the measurement of the ultrasonic motor's vibration in 1989. His current research interests are soft X-ray optical systems and soft X-ray detectors.

Mr. Miyake is a member of the Japan Society of Applied Physics.